High-Entropy Polyanionic Lithium Superionic Conductors

Florian Strauss, Jing Lin, Marie Duffiet, Kai Wang, Tatiana Zinkevich, Anna-Lena Hansen, Sylvio Indris, Torsten Brezesinski

ABSTRACT: High-entropy ceramics are attracting large interest because of their unique materials properties. Nevertheless, the effect of entropy on the lithium transport remains largely elusive. Here, we report, for the first time, about medium- and high-entropy polyanionic lithium superionic conductors crystallizing in the *F*–43*m* space group and adopting the so-called argyrodite structure. The $Li_6PS_5[Cl_{0.33}Br_{0.33}I_{0.33}]$, $Li_6P[S_{2.5}Se_{2.5}][Cl_{0.33}Br_{0.33}I_{0.33}]$, and $Li_{6.5}[Ge_{0.5}P_{0.5}][S_{2.5}Se_{2.5}][Cl_{0.33}Br_{0.33}I_{0.33}]$ materials were structurally characterized using complementary synchrotron and neutron scattering techniques in combination with ^{31}P magic-angle spinning (MAS) nuclear magnetic resonance (NMR) spectroscopy. We show that in contrast to other high-entropy ceramics, an unequal distribution of elements over the respective crystallographic sites occurs in these materials. Using electrochemical impedance spectroscopy (EIS) and ^{7}Li pulsed field gradient (PFG) NMR spectroscopy, we demonstrate that introducing entropy (compositional disorder) marginally affects the ionic conductivity (~10^{-3} S cm^{-1}), but instead lowers the activation energy for conduction to 0.22 eV. Our results emphasize the possibility of increasing entropy in polyanionic materials, thereby opening up compositional space for the search of Li-ion conductors with unprecedented properties.

In recent years, high-entropy materials (HEMs) are attracting significant research interest because of their often unexpected and tailorable properties. The high entropy concept is based on the idea of increasing configurational entropy, ΔS_{config}, in a specific structure type by introducing various elements on a single crystallographic site. Through possible manifold interactions between the incorporated elements, new materials properties arise or (in some cases) a certain lattice structure can be entropically stabilized.[1–3] Originally, the HEM concept emerged from high-entropy alloys (HEAs)[4,5] and has been extended to high-entropy ceramics (HECs). Both HEAs and HECs can adopt different crystal structures (e.g., rocksalt, perovskite, spinel, etc.), and configurational entropy is usually introduced via cation mixing (in ionic materials).[6–9] However, the high entropy concept has not yet been applied to polyanionic materials, despite their widespread use as electrode materials and ion conductors. An important feature of polyanionic-based materials is that they may offer a rigid three-dimensional framework, allowing for fast ion diffusion through interstitial space.[10–12] In principle, all ceramic oxide- and sulfide-based Li-ion conductors that are currently receiving interest, due to their potential for implementation as solid electrolytes (SEs) in solid-state batteries (SSBs), possess covalently bonded polyanions as building unit, such as $[PO_4]^{3-}$ or $[PS_4]^{3-}$.[13–16] Among them, lithium thiophosphates represent one of the most promising class of materials because of high ionic conductivity and favorable mechanical properties, ensuring intimate contact with the other battery components.[17–20] An example are the so-called argyrodites with the general formula Li_6PS_5X (X = Cl, Br, I), having $[PS_4]^{3-}$ tetrahedra along with uncoordinated X^- and S^{2-} anions and offering a structural framework for facile lithium diffusion.[21,22] Argyrodite SEs have been heavily investigated in the past, and indeed high ionic conductivity at room temperature has been achieved by substitution on the phosphorous, chalcogenide, and halide sites.[16,23–25] Thus, materials crystallizing in the argyrodite structure type seem capable of accommodating various elements simultaneously. This possibly allows for achieving a high ΔS_{config} and may provide insights on how configurational entropy alters the Li-ion transport properties. Note that increased lithium and proton conduction in high-entropy rocksalt oxides has been reported,[26,27] however, the effect that ΔS_{config} has on the charge transport remains unclear, and entropy was introduced by cation mixing only. In contrast, in the present work, we aimed at achieving high entropy primarily via anion mixing in the covalent/ionic host lattice of the argyrodite structure.

After synthetic survey of possible elements on the P, S, and X sites in Li_6PS_5X (with equimolar stoichiometry), we were able to successfully synthesize polyanionic (and cationic) materials, namely $Li_6PS_5[Cl_{0.33}Br_{0.33}I_{0.33}]$ (HEAR1), $Li_6P[S_{2.5}Se_{2.5}][Cl_{0.33}Br_{0.33}I_{0.33}]$ (HEAR2), and $Li_{6.5}[Ge_{0.5}P_{0.5}][S_{2.5}Se_{2.5}][Cl_{0.33}Br_{0.33}I_{0.33}]$ (HEAR3). First, the halide site, followed by the chalcogenide site, and finally the phosphorous site was substituted to successively alter (increase) the configurational entropy. Assuming equal distribution over the available crystallographic sites, ΔS_{config} values of 1.24R, 2.28R, and 2.98R were calculated for HEAR1, HEAR2, and HEAR3, respectively (see Supporting Information for details and **Table S1**). Materials for which $\Delta S_{config} \geq 1.5$ are usually considered high-entropy materials, originating from initial studies on HEAs, thus rendering HEAR2 and HEAR3 HEMs.[4,5] All materials were synthesized by classical solid-state chemistry with a high-energy milling step prior to annealing at temperatures of $\vartheta \geq 400$ °C in vacuum-sealed quartz ampoules (see Supporting Information for details). Initially, the elemental distribution

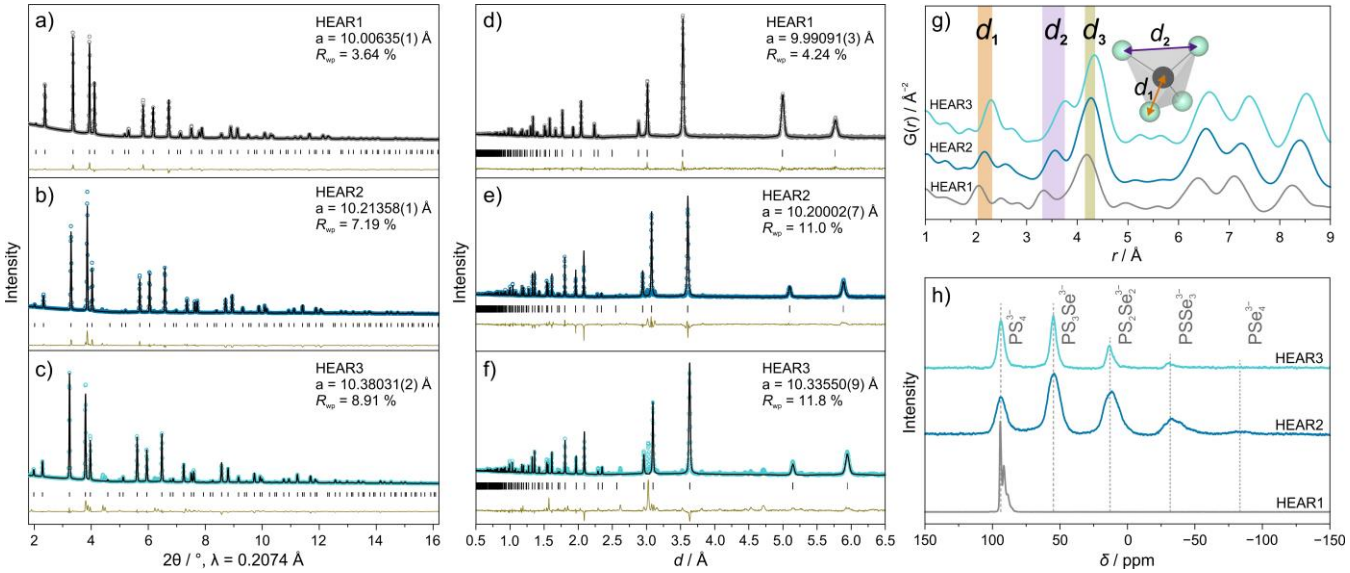

Figure 1. Structural characterization of the high-entropy lithium argyrodites. (a-c) SXRD and (d-f) NPD patterns and corresponding Rietveld refinement plots. The observed, calculated, and difference profiles are shown as colored circles, black lines, and beige lines, respectively. Vertical tick marks indicate the expected Bragg positions. (g) Corresponding PDF curves and (h) ^{31}P MAS NMR spectroscopy results.

on the nanometer level was probed using scanning transmission electron microscopy (STEM) combined with energy dispersive X-ray spectroscopy (EDS). As shown exemplarily for HEAR3 (see **Figure S1**), the as-synthesized material consists of micrometer-sized particles and all elements are uniformly distributed. To reveal the detailed crystal structure, synchrotron X-ray diffraction (SXRD) and time-of-flight neutron powder diffraction (NPD) measurements were conducted on the samples. As is evident from **Figure 1a-f**, the SXRD and NPD patterns can be indexed within the *F*–43*m* space group. The *a* lattice parameter increased linearly from about 10.0 Å for HEAR1 to 10.35 Å for HEAR3 (see **Figure S2**), thereby confirming the successful incorporation of Se and Ge.

Next, synchrotron X-ray total-scattering data were collected and pair distribution function (PDF) analysis conducted. The PDF curves (**Figure 1g**) show identical local structural features for the different materials. Three contributions can be attributed to the atomic distances around the (polyanionic) tetrahedral environment, $[PS_4]^{3-}$, $[PS_2Se_2]^{3-}$, and $[Ge_{0.5}P_{0.5}S_2Se_2]^{3.5-}$, as indicated in the inset. In particular, d_1 is assigned to the Ge/P–S/Se covalent bond within the tetrahedra and was found to increase from around 2.05 Å for HEAR1 to 2.29 Å for HEAR3. A similar trend was observed for d_2 (S/Se–S/Se) and d_3 (S/Se–S/Se), in agreement with the increase in *a* lattice parameter in the order of HEAR1 < HEAR2 < HEAR3. Note that d_2 refers to the S/Se–S/Se distance within the tetrahedra, whereas d_3 denotes the distance to the next-neighboring tetrahedra. The increase in local interatomic distances is consistent with the substitution of S and P with larger Se and Ge, respectively.

To further probe the phosphorous local environment, ^{31}P MAS NMR spectra were collected on the samples (**Figure 1h**). A narrow signal with some substructure was observed for HEAR1, indicating low local structural disorder. In contrast, four to five broad signals with different intensities were clearly visible for HEAR2 and HEAR3. This suggests a significant increase in local disorder compared to HEAR1. The chemical shift of the peaks can be explained by the different $[PS_{4-x}Se_x]^{3-}$ tetrahedra with x = 0 – 4. The substructure of the peak at +94 ppm for HEAR1, as well as at –30 ppm for HEAR2, is caused by the different arrangements of neighbors around these tetrahedra. Binominal fitting of the intensities allowed to quantitatively determine the overall number of x in $[PS_{4-x}Se_x]^{3-}$.[21,22] Naturally, for HEAR1, x = 0, as only $[PS_4]^{3-}$ units are present. However, for HEAR2 and HEAR3, x was calculated to equal 1.6 and 0.9, respectively, translating to $[PS_{2.4}Se_{1.6}]^{3-}$ and $[Ge_{0.5}P_{0.5}S_{3.1}Se_{0.9}]^{3.5-}$.

In addition, Raman spectroscopy measurements were conducted on the samples. The respective spectra display bands indicative of the polyanions, $[PS_{4-x}Se_x]^{3-}$ and $[GeS_{4-x}Se_x]^{4-}$ with x = 0 – 4 (see **Figure S3**).[28,29] For HEAR1, bands arising from the $[PS_4]^{3-}$ vibrations were clearly visible and centered around 416 and 575 cm^{-1}. These bands can be assigned to symmetric and asymmetric stretching vibrations of the $[PS_4]^{3-}$ tetrahedra, respectively.[29,30] For HEAR2, additional bands, due to the presence of different $[PS_{4-x}Se_x]^{3-}$ species, were present. However, in the case of HEAR3, the identification of single bands correlated with the $[PS_{4-x}Se_x]^{3-}$ and $[GeS_{4-x}Se_x]^{4-}$ tetrahedra is difficult because of strong overlapping. Nevertheless, as a starting point, the local structural information from ^{31}P MAS NMR spectroscopy was considered in the refinements.

HEAR1, HEAR2, and HEAR3 adopt the so-called argyrodite structure (**Figure 2a**), where anions form a face centered cubic sublattice (Wyckoff positions 4*a* and 4*d*) with chalcogenide anions in half of the tetrahedral voids (Wyckoff position 16*e*) and polyanionic tetrahedra on the octahedral sites (central atom on Wyckoff position 4*b*). The atoms located on the Wyckoff positions 4*a* (halide)

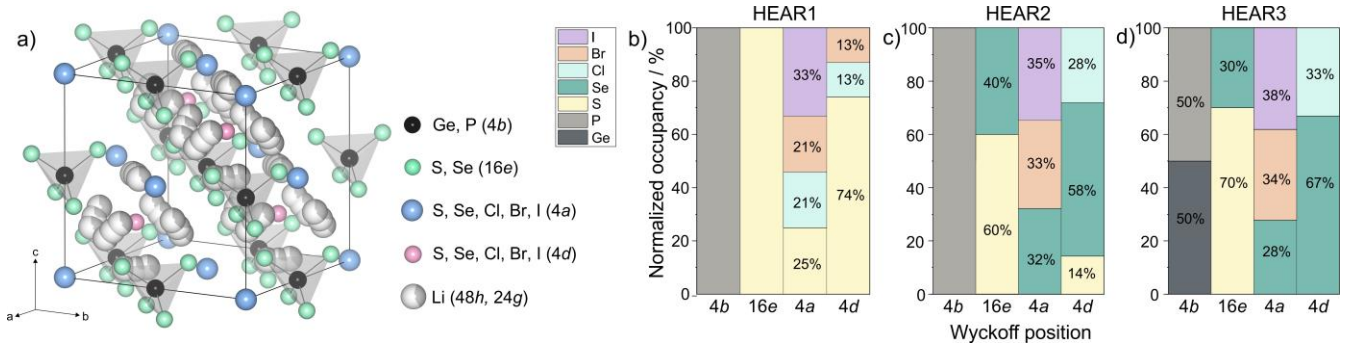

Figure 2. (a) Schematic view of the crystal structure of the high-entropy argyrodites. The different Wyckoff positions and elements are indicated. (b-d) Normalized occupancies of the different crystallographic sites, with the color referring to the elements displayed in the legend.

and 4*d* (chalcogenide) are known to distribute over both crystallographic sites, with is usually referred to as halide/chalcogenide site inversion. Moreover, the mobile cations (Li) are distributed around the 4*d* site, forming Frank-Kasper-polyhedra with two different Wyckoff positions (48*h* and 24*g*).[21,22] Thus, for the high-entropy argyrodite materials described in this work, the possible site inversion leads to large complexity. Through a combination of diffraction pattern simulation and subsequent Rietveld refinement, the detailed crystal structure could be determined (see Supporting Information for details). For the least complex material, HEAR1 (**Figure 2b**), the structure contains $[PS_4]^{3-}$ polyanions along with a rather equal occupation of the S (25%), Cl (21%), Br (21%), and I (33%) on the 4*a* site. We also noticed some halide/chalcogenide mixing, since on the 4*d* site, 13% Br and 13% Cl were found (apart from 74% S). This kind of site inversion (Cl/Br and S) is often observed in lithium argyrodites, whereas I typically does not tend to share occupancy with S because of the large difference in ionic radii.[21,22] For HEAR2 (**Figure 2c**), additionally, half of the S was substituted with Se. In agreement with the results from the ^{31}P MAS NMR spectroscopy measurements, we found 60% S and 40% Se on the 16*e* site, forming $[PS_{2.4}Se_{1.6}]^{3-}$ tetrahedra. The 4*a* size contained virtually equal amounts of I (35%), Br (33%), and Se (32%). In contrast, Cl (28%) was solely present on the 4*d* site along with Se (58%) and S (14%). In contrast to HEAR1, Cl is pushed to the 4*d* site, with both I and Br remaining on the 4*a* site. Such elemental mixing on the 4*a* and 4*d* Wyckoff positions is most likely the result of mismatch and/or similarities in ionic radii. For HEAR3, a comparable distribution over the different crystallographic sites as for HEAR2 was observed (**Figure 2d**). The most noticeable difference is that $[Ge_{0.5}P_{0.5}S_{2.8}Se_{1.2}]^{3.5-}$ tetrahedra were present, meaning 70% S and 30% Se on the 16*e* site, in fair agreement with the S/Se ratio determined by ^{31}P MAS NMR spectroscopy. On the 4*a* and 4*d* sites, 38% I/34% Br/28% Se and 33% Cl/67% Se, respectively, were found. Taken together, the refinement of the partial atomic occupancies is in accordance with the targeted stoichiometries, except for HEAR3, where a slight deviation from the original S/Se ratio, $Li_{6.5}[Ge_{0.5}P_{0.5}][S_{2.8}Se_{2.2}][Cl_{0.33}Br_{0.34}I_{0.38}]$, was observed. This might also be the reason for the presence of clear impurity reflections in the SXRD and NPD patterns (**Figure 1c**,**f**).

In conclusion, substituting S with Se does not significantly increase the halide/chalcogenide site disorder. However, in this case, selective Cl/Se mixing on the 4*d* Wyckoff position occurs (**Figure 2c**,**d**), with the I and Br remaining on the halide 4*a* site. We hypothesize that the unequal mixing over the 4*a* and 4*d* sites, as seen for HEAR2 and HEAR3, is a result of minimizing the lattice distortion by keeping the difference in ionic radii ≤ 12% (for a specific crystallographic position). As known for argyrodites, altering the anion (and cation) sublattice causes a change in the Li substructure. Usually, Li can be distributed over two different Wyckoff positions, 48*h* and 24*g*. Rietveld refinement analysis of the NPD data showed that Li is mainly located on the 48*h* site (HEAR1, 93%), the fraction of which increased further for HEAR2 (95%) and HEAR3 (100%), see **Figure S4a**. Moreover, the Li^+–Li^+ jump distances remained virtually unaltered upon changing the anion and cation sublattices (see **Figure S4b**).

After having examined the crystal structure, the Li-ion conductivity of the as-prepared materials was probed using EIS. EIS measurements were conducted at different temperatures on sintered pellets with deposited gold electrodes. All samples showed a partial semicircle and a capacitive tail, indicating primarily ionic conductivity (see **Figure S5**). From the measured resistance, the conductivity was determined (**Figure 3a**). At 25 °C, values of 0.7, 1.3, and 1.1 mS cm^{-1} were calculated for HEAR1, HEAR2, and HEAR3, respectively. The evolution of conductivity with temperature follows an Arrhenius-type behavior with very similar activation energies of 0.29 for HEAR1 and 0.31 eV for both HEAR2 and HEAR3. Consequently, no significant changes in conductivity and activation energy for conduction were observed with increasing compositional disorder. However, because EIS measurements probe the overall sample conductivity (pellet specimen), the results can be assumed to be affected by grain-boundary effects or crystalline/amorphous impurities.[31,32] For this reason, ^{7}Li PFG NMR spectroscopy measurements were conducted on the materials at different temperatures and at a diffusion time of 100 ms. In so doing, the lithium-diffusion coefficient, D_{Li}, can be determined (**Figure 3b**), from which the Li-ion conductivity is derived via the Nernst-Einstein equation. For HEAR1, HEAR2, and HEAR3, D_{Li} at 25 °C was found to be $0.99 \cdot 10^{-12}$, $1.13 \cdot 10^{-12}$, and $0.74 \cdot 10^{-12}$ m^2 s^{-1}, respectively, in the range usually observed for superionic conductors.[33,34] From

these values, ionic conductivities of 1.7, 1.8, and 1.2 mS cm^{-1}, respectively, were calculated.

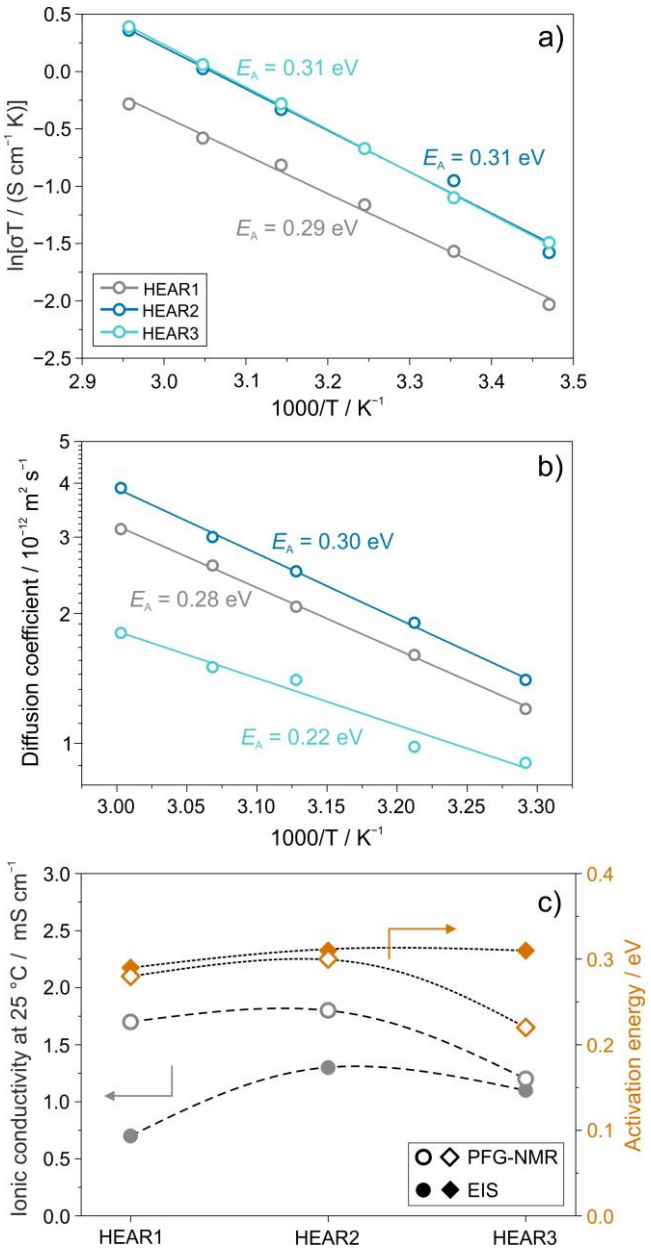

Figure 3. (a) Arrhenius fitting of the ionic conductivity in the temperature range from 15 to 65 °C. (b) Temperature-dependent diffusion coefficient from ^{7}Li PFG NMR spectroscopy. (c) Summary plot of the ionic conductivities and corresponding activation energies at 25 °C determined from EIS and ^{7}Li PFG NMR spectroscopy measurements.

The change in D_{Li} also follows an Arrhenius-type behavior, and the activation energies for conduction for HEAR1 (0.28 eV) and HEAR2 (0.30 eV) are very similar to those determined from the EIS measurements. However, for HEAR3, a lower activation energy was calculated compared to EIS (0.22 vs 0.31 eV). An overview of the ionic conductivities and activation energies for the different materials is given in **Figure 3c**. As is evident, there are two main discrepancies between the EIS and ^{7}Li PFG NMR spectroscopy measurements. First, for HEAR1, the conductivity determined by ^{7}Li PFG NMR spectroscopy is more than twice that from EIS. This is probably due to the presence of crystalline/amorphous side phases, as ^{7}Li PFG NMR spectroscopy probes the bulk material, whereas EIS measures the overall sample conductivity. Second, although the conductivity of HEAR3 from EIS and ^{7}Li PFG NMR spectroscopy is similar, the activation energy for conduction is different. We hypothesize that this difference is also related to the presence of (unknown) impurities, having a more pronounced effect on the EIS data. Similar observations have been made for thiophosphate-based solid electrolytes.[31,32,35]

Taken together, the results indicate that the room-temperature Li-ion conductivity and activation energy (from ^{7}Li PFG NMR spectroscopy) are almost identical for the purely polyanionic high-entropy argyrodite materials, HEAR1 and HEAR2. However, upon additional cation substitution (HEAR3), both the ionic conductivity and activation energy decreased, leading to the lowest value reported for argyrodite-type Li-ion conductors (0.22 eV).[16,24] The activation energy was found to be linearly correlated with the pre-exponential factor of the diffusivity, D_0, known as the Meyer-Neldel rule (see **Figure S6**).[36,37] This suggests softening of the lattice with increasing configurational entropy,[38,39] which negatively affects the bulk ion transport in the case of HEAR3. Moreover, XRD and NPD revealed similar structural features for all three materials, i.e., a comparable halide/chalcogenide site inversion, ranging from 26 to 33%, and minor changes in the Li substructure.

In summary, we have reported about the successful synthesis of multi-element substituted lithium argyrodites with a high ΔS_{config}. This was mainly achieved through anion mixing. Although nominally equal amounts of elemental constituents were used, non-uniform mixing over the respective crystallographic sites was observed, unlike for many other HEMs. Thus, the real ΔS_{config} values can be assumed to be smaller than the calculated ones (see **Table S1**). The Li-ion conductivity (10^{-3} S cm^{-1}) was not strongly affected by increasing compositional disorder (configurational entropy). However, low activation energies for conduction (≤0.31 eV) were found. The former is most likely due to close structural similarities between the investigated samples. Nevertheless, increasing the number of elements alters both the configurational entropy and the vibrational entropy (lattice softening), which may have synergistic or antagonistic effects on charge transport.[7,37,40] Distinguishing between these two entropy contributions (and ultimately from structural effects) remains challenging.

Overall, we believe that our study triggers further research into high-entropy ion conductors, potentially allowing for tailoring the electrical and (electro)chemical properties. This is a clear advantage considering the large compositional design space available for exploration.

ASSOCIATED CONTENT

Supporting Information. Materials and characterization. Calculation of configurational entropy. STEM-EDS images. Structural parameters and Li occupancies. Raman and EIS spectra. Pre-exponential factor of the diffusivity versus activation energy. LeBail fit for the Li_2Se precursor. This material is available free of charge via the Internet at http://pubs.acs.org.

AUTHOR INFORMATION

Corresponding Authors

Florian Strauss – Battery and Electrochemistry Laboratory, Institute of Nanotechnology, Karlsruhe Institute of Technology (KIT), Hermann-von-Helmholtz-Platz 1, 76344 Eggenstein-Leopoldshafen, Germany; orcid.org/0000-0001-5817-6349; Email: florian.strauss@kit.edu

Torsten Brezesinski – Battery and Electrochemistry Laboratory, Institute of Nanotechnology, Karlsruhe Institute of Technology (KIT), Hermann-von-Helmholtz-Platz 1, 76344 Eggenstein-Leopoldshafen, Germany; orcid.org/0000-0002-4336-263X; Email: torsten.brezesinski@kit.edu

Authors

Jing Lin – Battery and Electrochemistry Laboratory, Institute of Nanotechnology, Karlsruhe Institute of Technology (KIT), Hermann-von-Helmholtz-Platz 1, 76344 Eggenstein-Leopoldshafen, Germany

Marie Duffiet – Battery and Electrochemistry Laboratory, Institute of Nanotechnology, Karlsruhe Institute of Technology (KIT), Hermann-von-Helmholtz-Platz 1, 76344 Eggenstein-Leopoldshafen, Germany

Kai Wang – Institute of Nanotechnology, Karlsruhe Institute of Technology (KIT), Hermann-von-Helmholtz-Platz 1, 76344 Eggenstein-Leopoldshafen, Germany

Tatiana Zinkevich – Institute for Applied Materials-Energy Storage Systems, Karlsruhe Institute of Technology (KIT), Hermann-von-Helmholtz-Platz 1, 76344 Eggenstein-Leopoldshafen, Germany; Helmholtz Institute Ulm (HIU) Electrochemical Energy Storage, 89081 Ulm, Germany

Anna-Lena Hansen – Institute for Applied Materials-Energy Storage Systems, Karlsruhe Institute of Technology (KIT), Hermann-von-Helmholtz-Platz 1, 76344 Eggenstein-Leopoldshafen, Germany

Sylvio Indris – Institute for Applied Materials-Energy Storage Systems, Karlsruhe Institute of Technology (KIT), Hermann-von-Helmholtz-Platz 1, 76344 Eggenstein-Leopoldshafen, Germany; Helmholtz Institute Ulm (HIU) Electrochemical Energy Storage, 89081 Ulm, Germany

Notes

The authors declare no competing financial interest.

Acknowledgement

F.S. is grateful to the Fonds der Chemischen Industrie for financial support through a Liebig fellowship. J.L. acknowledges the FCI for PhD funding. This work was partially supported by BASF SE. This research used resources at the Spallation Neutron Source (SNS), a DOE Office of Science User Facility operated by the Oak Ridge National Laboratory (ORNL). We acknowledge DESY (Hamburg, Germany), a member of the Helmholtz Association HGF, for the provision of experimental facilities. Parts of this research were carried out at PETRA III, and we would like to thank Volodymyr Baran for assistance in using beamline P02.1.

REFERENCES

(1) Oses, C.; Toher, C.; Curtarolo, S. High-Entropy Ceramics. *Nat. Rev. Mater.* **2020**, *5*, 295–309.

(2) Rost, C. M.; Sachet, E.; Borman, T.; Moballegh, A.; Dickey, E. C.; Hou, D.; Jones, J. L.; Curtarolo, S.; Maria, J.-P. Entropy-Stabilized Oxides. *Nat. Commun.* **2015**, *6*, 8485.

(3) Chen, Y.; Fu, H.; Huang, Y.; Huang, L.; Zheng, X.; Dai, Y.; Huang, Y.; Luo, W. Opportunities for High-Entropy Materials in Rechargeable Batteries. *ACS Mater. Lett.* **2021**, *3*, 160–170.

(4) George, E. P.; Raabe, D.; Ritchie, R. O. High-Entropy Alloys. *Nat. Rev. Mater.* **2019**, *4*, 515–534.

(5) *High-Entropy Alloys*; Gao, M. C., Yeh, J.-W., Liaw, P. K., Zhang, Y., Eds.; Springer International Publishing: Cham, **2016**.

(6) Sarkar, A.; Wang, Q.; Schiele, A.; Chellali, M. R.; Bhattacharya, S. S.; Wang, D.; Brezesinski, T.; Hahn, H.; Velasco, L.; Breitung, B. High-Entropy Oxides: Fundamental Aspects and Electrochemical Properties. *Adv. Mater.* **2019**, *31*, 1806236.

(7) Zhang, R.-Z.; Reece, M. J. Review of High Entropy Ceramics: Design, Synthesis, Structure and Properties. *J. Mater. Chem. A* **2019**, *7*, 22148–22162.

(8) High Entropy Oxides: The Role of Entropy, Enthalpy and Synergy. *Scr. Mater.* **2020**, *187*, 43–48.

(9) Ma, Y.; Ma, Y.; Wang, Q.; Schweidler, S.; Botros, M.; Fu, T.; Hahn, H.; Brezesinski, T.; Breitung, B. High-Entropy Energy Materials: Challenges and New Opportunities. *Energy Environ. Sci.* **2021**, *14*, 2883–2905.

(10) Masquelier, C.; Croguennec, L. Polyanionic (Phosphates, Silicates, Sulfates) Frameworks as Electrode Materials for Rechargeable Li (or Na) Batteries. *Chem. Rev.* **2013**, *113*, 6552–6591.

(11) Gong, Z.; Yang, Y. Recent Advances in the Research of Polyanion-Type Cathode Materials for Li-Ion Batteries. *Energy Environ. Sci.* **2011**, *4*, 3223–3242.

(12) Jin, T.; Li, H.; Zhu, K.; Wang, P.-F.; Liu, P.; Jiao, L. Polyanion-Type Cathode Materials for Sodium-Ion Batteries. *Chem. Soc. Rev.* **2020**, *49*, 2342–2377.

(13) Zhang, Z.; Shao, Y.; Lotsch, B.; Hu, Y.-S.; Li, H.; Janek, J.; Nazar, L. F.; Nan, C.-W.; Maier, J.; Armand, M. New Horizons for Inorganic Solid State Ion Conductors. *Energy Environ. Sci.* **2018**, *11*, 1945–1976.

(14) Reddy, M. V.; Julien, C. M.; Mauger, A.; Zaghib, K. Sulfide and Oxide Inorganic Solid Electrolytes for All-Solid-State Li Batteries: A Review. *Nanomaterials* **2020**, *10*, 1606.

(15) Park, K. H.; Bai, Q.; Kim, D. H.; Oh, D. Y.; Zhu, Y.; Mo, Y.; Jung, Y. S. Design Strategies, Practical Considerations, and New Solution Processes of Sulfide Solid Electrolytes for All-Solid-State Batteries. *Adv. Energy Mater.* **2018**, *8*, 1800035.

(16) Bachman, J. C.; Muy, S.; Grimaud, A.; Chang, H.-H.; Pour, N.; Lux, S. F.; Paschos, O.; Maglia, F.; Lupart, S.; Lamp, P.; Giordano, L.; Shao-Horn, Y. Inorganic Solid-State Electrolytes for Lithium Batteries: Mechanisms and Properties Governing Ion Conduction. *Chem. Rev.* **2016**, *116*, 140–162.

(17) Kato, Y.; Hori, S.; Saito, T.; Suzuki, K.; Hirayama, M.; Mitsui, A.; Yonemura, M.; Iba, H.; Kanno, R. High-Power All-Solid-State Batteries Using Sulfide Superionic Conductors. *Nat. Energy* **2016**, *1*, 16030.

(18) Lau, J.; DeBlock, R. H.; Butts, D. M.; Ashby, D. S.; Choi, C. S.; Dunn, B. S. Sulfide Solid Electrolytes for Lithium Battery Applications. *Adv. Energy Mater.* **2018**, *8*, 1800933.

(19) Teo, J. H.; Strauss, F.; Walther, F.; Ma, Y.; Payandeh, S.; Scherer, T.; Bianchini, M.; Janek, J.; Brezesinski, T. The Interplay between (Electro)chemical and (Chemo)mechanical Effects in the Cycling Performance of Thiophosphate-Based Solid-State Batteries. *Mater. Futures* **2022**, *1*, 015102.

(20) Teo, J. H.; Strauss, F.; Tripković, Đ.; Schweidler, S.; Ma, Y.; Bianchini, M.; Janek, J.; Brezesinski, T. Design-of-Experiments-Guided Optimization of Slurry-Cast Cathodes for Solid-State Batteries. *Cell Rep. Phys. Sci.* **2021**, *2*, 100465.

(21) Deiseroth, H.-J.; Kong, S.-T.; Eckert, H.; Vannahme, J.; Reiner, C.; Zaiß, T.; Schlosser, M. Li_6PS_5X: A Class of Crystalline Li-Rich Solids With an Unusually High Li^+ Mobility. *Angew. Chem. Int. Ed.* **2008**, *47*, 755–758.

(22) Kong, S.-T.; Deiseroth, H.-J.; Reiner, C.; Gün, Ö.; Neumann, E.; Ritter, C.; Zahn, D. Lithium Argyrodites with Phosphorus and Arsenic: Order and Disorder of Lithium Atoms, Crystal Chemistry, and Phase Transitions. *Chem. Eur. J.* **2010**, *16*, 2198–2206.

(23) Yu, C.; Zhao, F.; Luo, J.; Zhang, L.; Sun, X. Recent Development of Lithium Argyrodite Solid-State Electrolytes for Solid-State Batteries: Synthesis, Structure, Stability and Dynamics. *Nano Energy* **2021**, *83*, 105858.

(24) Bai, X.; Duan, Y.; Zhuang, W.; Yang, R.; Wang, J. Research Progress in Li-Argyrodite-Based Solid-State Electrolytes. *J. Mater. Chem. A* **2020**, *8*, 25663–25686.

(25) Zhou, L.; Minafra, N.; Zeier, W. G.; Nazar, L. F. Innovative Approaches to Li-Argyrodite Solid Electrolytes for All-Solid-State Lithium Batteries. *Acc. Chem. Res.* **2021**, *54*, 2717–2728.

(26) Bérardan, D.; Franger, S.; Meena, A. K.; Dragoe, N. Room Temperature Lithium Superionic Conductivity in High Entropy Oxides. *J. Mater. Chem. A* **2016**, *4*, 9536–9541.

(27) Gazda, M.; Miruszewski, T.; Jaworski, D.; Mielewczyk-Gryń, A.; Skubida, W.; Wachowski, S.; Winiarz, P.; Dzierzgowski, K.; Łapiński, M.; Szpunar, I.; Dzik, E. Novel Class of Proton Conducting Materials—High Entropy Oxides. *ACS Mater. Lett.* **2020**, *2*, 1315–1321.

(28) Marple, M. A. T.; Aitken, B. G.; Kim, S.; Sen, S. Observation of a Phonon Softening Effect on Li Ion Conduction in Mixed-Anion Chalcogenide Glasses. *Chem. Mater.* **2018**, *30*, 5896–5903.

(29) Krauskopf, T.; Muy, S.; Culver, S. P.; Ohno, S.; Delaire, O.; Shao-Horn, Y.; Zeier, W. G. Comparing the Descriptors for Investigating the Influence of Lattice Dynamics on Ionic Transport Using the Superionic Conductor $Na_3PS_{4-x}Se_x$. *J. Am. Chem. Soc.* **2018**, *140*, 14464–14473.

(30) Pätzmann, U.; Brockner, W. Schwingungsspektren von Ag_3PS_4 und Cu_3PS_4 / Vibrational Spectra of Ag_3PS_4 and Cu_3PS_4. *Z. Naturforschung A* **1983**, *38*, 27–30.

(31) Harm, S.; Hatz, A.-K.; Moudrakovski, I.; Eger, R.; Kuhn, A.; Hoch, C.; Lotsch, B. V. Lesson Learned from NMR: Characterization and Ionic Conductivity of LGPS-like Li_7SiPS_8. *Chem. Mater.* **2019**, *31*, 1280–1288.

(32) Morales, D. J.; Greenbaum, S. NMR Investigations of Crystalline and Glassy Solid Electrolytes for Lithium Batteries: A Brief Review. *Int. J. Mol. Sci.* **2020**, *21*, 3402.

(33) Kuhn, A.; Duppel, V.; Lotsch, B. V. Tetragonal Li10GeP2S12 and Li_7GePS_8 – Exploring the Li Ion Dynamics in LGPS Li Electrolytes. *Energy Environ. Sci.* **2013**, *6*, 3548–3552.

(34) Adeli, P.; Bazak, J. D.; Park, K. H.; Kochetkov, I.; Huq, A.; Goward, G. R.; Nazar, L. F. Boosting Solid-State Diffusivity and Conductivity in Lithium Superionic Argyrodites by Halide Substitution. *Angew. Chem. Int. Ed.* **2019**, *58*, 8681–8686.

(35) Holzmann, T.; Schoop, L. M.; Ali, M. N.; Moudrakovski, I.; Gregori, G.; Maier, J.; Cava, R. J.; Lotsch, B. V. $Li_{0.6}[Li_{0.2}Sn_{0.8}S_2]$ – a Layered Lithium Superionic Conductor. *Energy Environ. Sci.* **2016**, *9*, 2578–2585.

(36) Gelin, S.; Champagne-Ruel, A.; Mousseau, N. Enthalpy-Entropy Compensation of Atomic Diffusion Originates from Softening of Low Frequency Phonons. *Nat. Commun.* **2020**, *11*, 3977.

(37) Muy, S.; Bachman, J. C.; Giordano, L.; Chang, H.-H.; Abernathy, D. L.; Bansal, D.; Delaire, O.; Hori, S.; Kanno, R.; Maglia, F.; Lupart, S.; Lamp, P.; Shao-Horn, Y. Tuning Mobility and Stability of Lithium Ion Conductors Based on Lattice Dynamics. *Energy Environ. Sci.* **2018**, *11*, 850–859.

(38) Körmann, F.; Ikeda, Y.; Grabowski, B.; Sluiter, M. H. F. Phonon Broadening in High Entropy Alloys. *Npj Comput. Mater.* **2017**, *3*, 36.

(39) Kraft, M. A.; Culver, S. P.; Calderon, M.; Böcher, F.; Krauskopf, T.; Senyshyn, A.; Dietrich, C.; Zevalkink, A.; Janek, J.; Zeier, W. G. Influence of Lattice Polarizability on the Ionic Conductivity in the Lithium Superionic Argyrodites Li_6PS_5X (X = Cl, Br, I). *J. Am. Chem. Soc.* **2017**, *139*, 10909–10918.

(40) Phani Dathar, G. K.; Balachandran, J.; Kent, P. R. C.; Rondinone, A. J.; Ganesh, P. Li-Ion Site Disorder Driven Superionic Conductivity in Solid Electrolytes: A First-Principles Investigation of β-Li_3PS_4. *J. Mater. Chem. A* **2017**, *5*, 1153–1159.

TOC Graphic